

Electronic Supporting Information

V₅S₈-graphite hybrid nanosheets as a high-capacity and cycle-stable anode material for sodium-ion batteries

Chenghao Yang,^{*a} Xing Ou,^a Xunhui Xiong,^a Fenghua Zheng,^a Renzong Hu,^b Yu Chen,^b Meilin Liu^{ab} and Kevin Huang^{*c}

^a New Energy Research Institute, School of Environment and Energy, South China University of Technology, Guangzhou 510006, P.R. China.

E-mail: esyangc@scut.edu.cn (C. Yang)

^b School of Materials Science & Engineering, Georgia Institute of Technology, Atlanta, GA30332-0245, USA

^c Department of Mechanical Engineering, University of South Carolina, Columbia, SC 29205, USA

E-mail: huang46@cec.sc.edu (K. Huang)

Experimental

1. Material synthesis

Synthesis of the bulk V_5S_8 materials. The bulk V_5S_8 (b- V_5S_8) material was synthesized by a conventional solid-state sulfidization route, *i.e.* mixing V_2O_5 (Aldrich >99%) with sulfur powders (Aldrich >99%) in a stoichiometric ratio of 1:5 (see Fig. S3).^{S1,S2} The mixture was then ball milled under an argon atmosphere for 3 h with milling ball (polyurethane) to powder ratio of 10:1. The rotation speed of the mill was set to 400 rpm to ensure an intimate mixing. Then, 5g S and 1 g ball-milled raw materials mixture were loaded into two individual ceramic boats, and placed in the upstream and middle side of the tubular furnace, respectively, as schematically shown in Fig. S3. The samples were annealed at 200 °C for 1 h initially, and then calcined at 750 °C for 2 h with a heating rate of 5 °C min⁻¹ in a H₂ (8%)-Ar (92%) atmosphere. After cooling to room temperature, black b- V_5S_8 powders were obtained.

Synthesis of the chemically exfoliated V_5S_8 (ce- V_5S_8) and V_5S_8 -C hybrid nanosheets. The ce- V_5S_8 nanosheets were prepared by a facile chemical exfoliation method. A 500 mg of the synthesized bulk V_5S_8 powders and 2.5 mg NaOH were first added into a 12 mL flask, and then a 10 mL of N-methyl-2-pyrrolidone (NMP) was added as the dispersion solvent. The flask was sealed and the mixture was sonicated in ice-bath for 4 h. After centrifuging at 5000 rpm for 10 min, the sediments containing the unexfoliated V_5S_8 or thick flakes were removed. Finally, the remaining supernatants were filtered and washed by deionized (DI) water to obtain the ce- V_5S_8 . Meanwhile, the b- V_5S_8 powders were also mechanically mixed with graphite by ball milling (b- V_5S_8 -C). Last, the chemically exfoliated V_5S_8 -C (ce- V_5S_8 -C) nanosheets were prepared by the same process as that of ce- V_5S_8 nanosheets described above, with a mass ratio of b- V_5S_8 powders to graphite at 17:3.

Synthesis of the chemically exfoliated VS_2 nanosheets. VS_2 powders were synthesized

by a hydrothermal method as reported elsewhere.²² In a typical experiment, 4 mmole ammonium metavanadate (NH_4VO_3) and 20 mmole thioacetamide (CH_3CSNH_2) were first dissolved in 70 mL DI water, which was then vigorously stirred until the NH_4VO_3 was completely dissolved. The solution was transferred into a 100 mL Teflon-lined stainless steel autoclave, sealed and annealed at 180 °C for 20 h. After cooling down to room temperature, the black precipitate was collected by centrifugation and washed for several times with ethanol and DI water, followed by drying in vacuum oven at 80°C for 10 h to obtain the bulk VS_2 (b- VS_2) powders. Finally, the VS_2 nanosheets (ce- VS_2) were prepared by the same chemical exfoliation process as described above.

2. Material characterizations

The X-ray diffraction (XRD) measurements were performed on the Bruker D8 Advance (Germany) using Cu $K\alpha$ radiation (1.5405 Å) in 0.02° increments between 10° and 80° at a scanning speed of 0.08° per second. Thermal analysis was performed using STA-449C (Netzsch, Germany) in a temperature range of 50 to 900°C with a heating rate of 10°C min⁻¹. Raman spectroscopy was carried out at a wavelength of 514 nm using a high resolution dispersive Raman spectroscopy (Horiba JobinYvon, ARAMIS). Microstructure of the samples was captured with scanning electron microscopy (SEM, FEI Quanta 200 FEG), and the chemistry on the surface of samples were examined by energy-dispersive X-ray spectroscopy (EDX). The morphology of power samples were also observed with a high-resolution transmission electron microscopy (HRTEM, Tecnai G2 F20 S-TWIN, Japan) operating at 200 KV.

For *in situ* XRD experiments, the configuration of the *in situ* battery cell is described in detail in Fig. S4, which is consisted of a 12 mm inner diameter electrochemical cell with a Be window for x-ray transmission and carbon paper as a current collector. Each scan was collected in 0.02° increments between 10° and 50° at a scanning speed of 0.04° per second. The time

interval for each scan was set for 180 seconds, to ensure enough time to trace the reaction during the charge/discharge process.

3. Electrochemical evaluation

Electrochemical evaluations of the anode materials were performed using 2032-type coin cells. Electrodes were prepared by mixing the as-prepared ce-VS₂, ce-V₅S₈ or ce-V₅S₈-C composites with carbon black and polyvinylidene difluoride in a weight ratio of 70:20:10 in NMP solvent. The diameter of the electrode roundels is 12 mm, and the loaded active electrode materials are about 1.0 mg cm⁻². SIBs were assembled with sodium tablet as the counter electrode, 1 M NaClO₄ in propylene carbonate solution as the electrolyte, and Whatman glass papers as the separator. For comparison, LIBs were fabricated at the same conditions, but using lithium as counterpart, 1 M LiPF₆ in a mixture of ethylene carbonate/dimethyl carbonate/ethylmethyl carbonate (EC/DMC/EMC, 1:1:1 in volume ratio) solution as the electrolyte and Celguard 2400 microporous polyethylene membrane as a separator. The charge-discharge cycling was galvanostatically performed at room temperature with a desired current density. The specific capacity (mAh g⁻¹) of the electrodes was evaluated based on the total mass of electrode materials (ce-VS₂, ce-V₅S₈ and ce-V₅S₈-C). The mass loading of ce-VS₂, ce-V₅S₈ and ce-V₅S₈-C in the electrodes is controlled to be 0.77 mg. In particular, for ce-V₅S₈-C, it contains 0.655 mg ce-V₅S₈ and 0.115 mg graphite. Cyclic voltammetry (CV) measurements were performed using a CHI660A electrochemical workstation at a scan rate of 0.1 mV s⁻¹ from 0.01 to 3.0 V. Electrochemical impedance spectra (EIS) were acquired using a Solartron 1287 electrochemical interface equipped with 1255B frequency analyzer at a perturbation voltage of 5 mV over a frequency range of 100 kHz - 0.01 Hz.

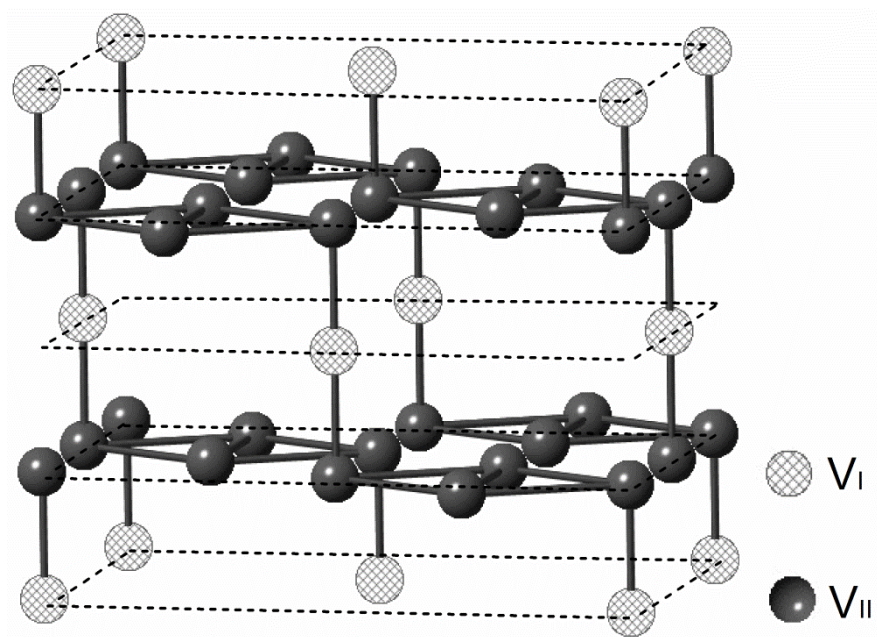


Fig. S1 Arrangement of V atoms in V_5S_8 .

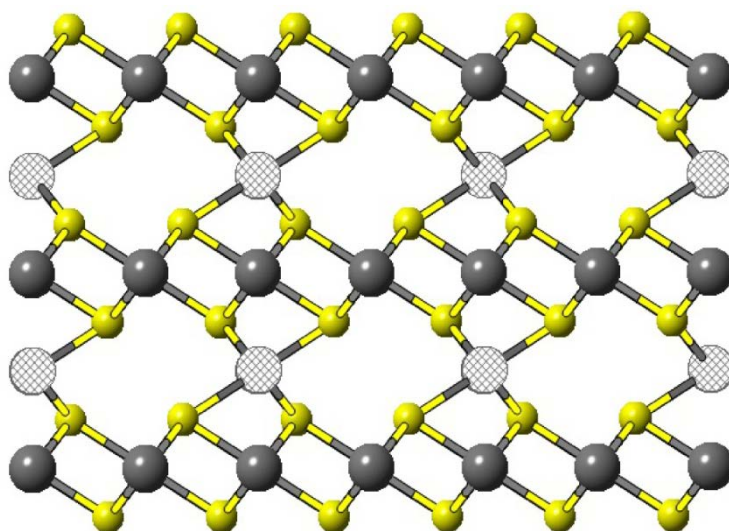


Fig. S2 Side view of the V and S atoms arrangement in V_5S_8 . The gray balls (V_I) and hollow hatched gray balls (V_{II}) are V atoms, and the yellow balls are S atoms.

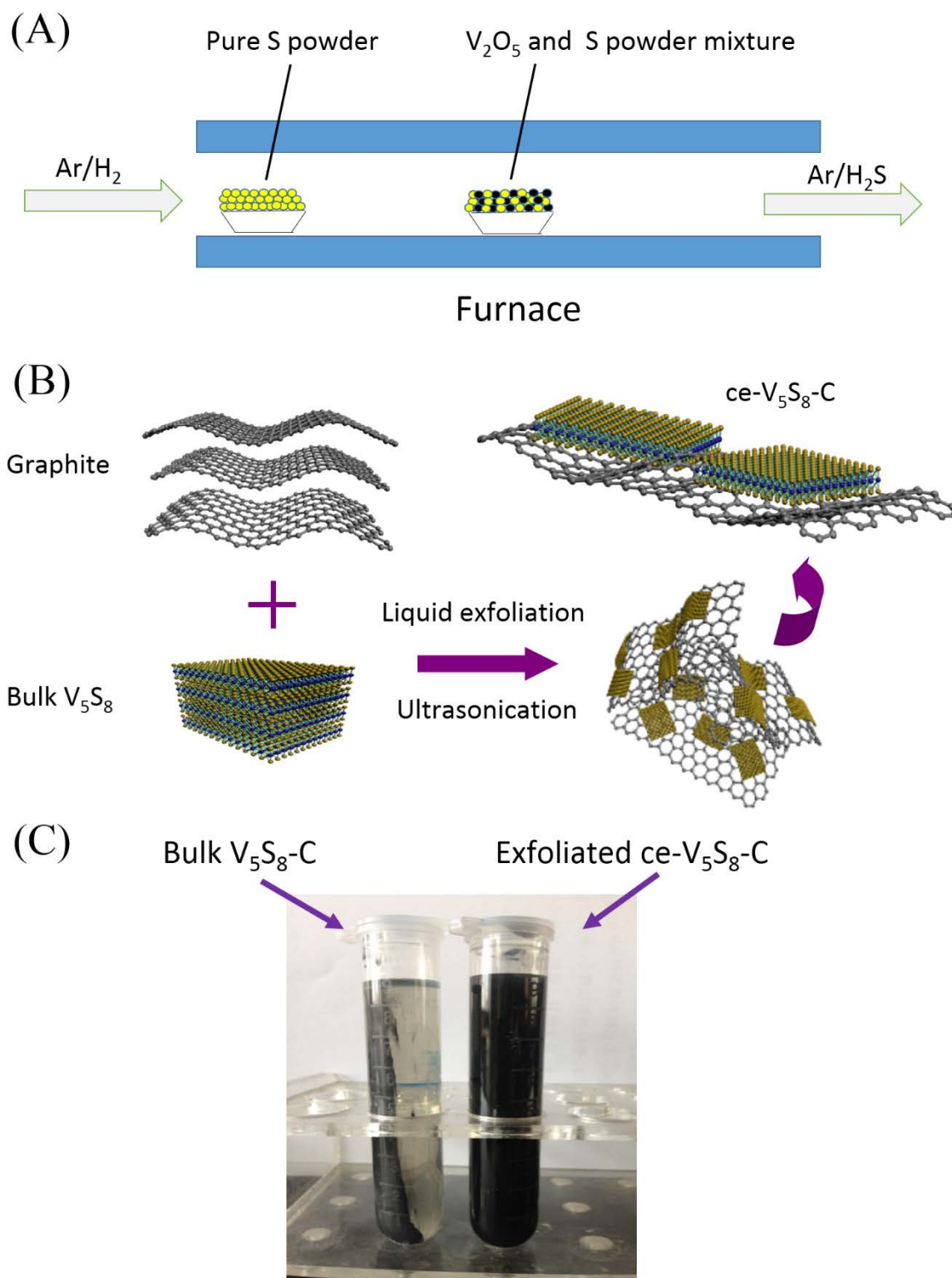


Fig. S3 Schematic illustration of fabrication of bulk V_5S_8 (b- V_5S_8) by a conventional solid-state sulfidization route (A), schematic illustration the preparation of V_5S_8 with chemical exfoliation method (ce- V_5S_8 -C) (B), and photographs of bulk and exfoliated dispersions after centrifugation at 5000 rpm (C).

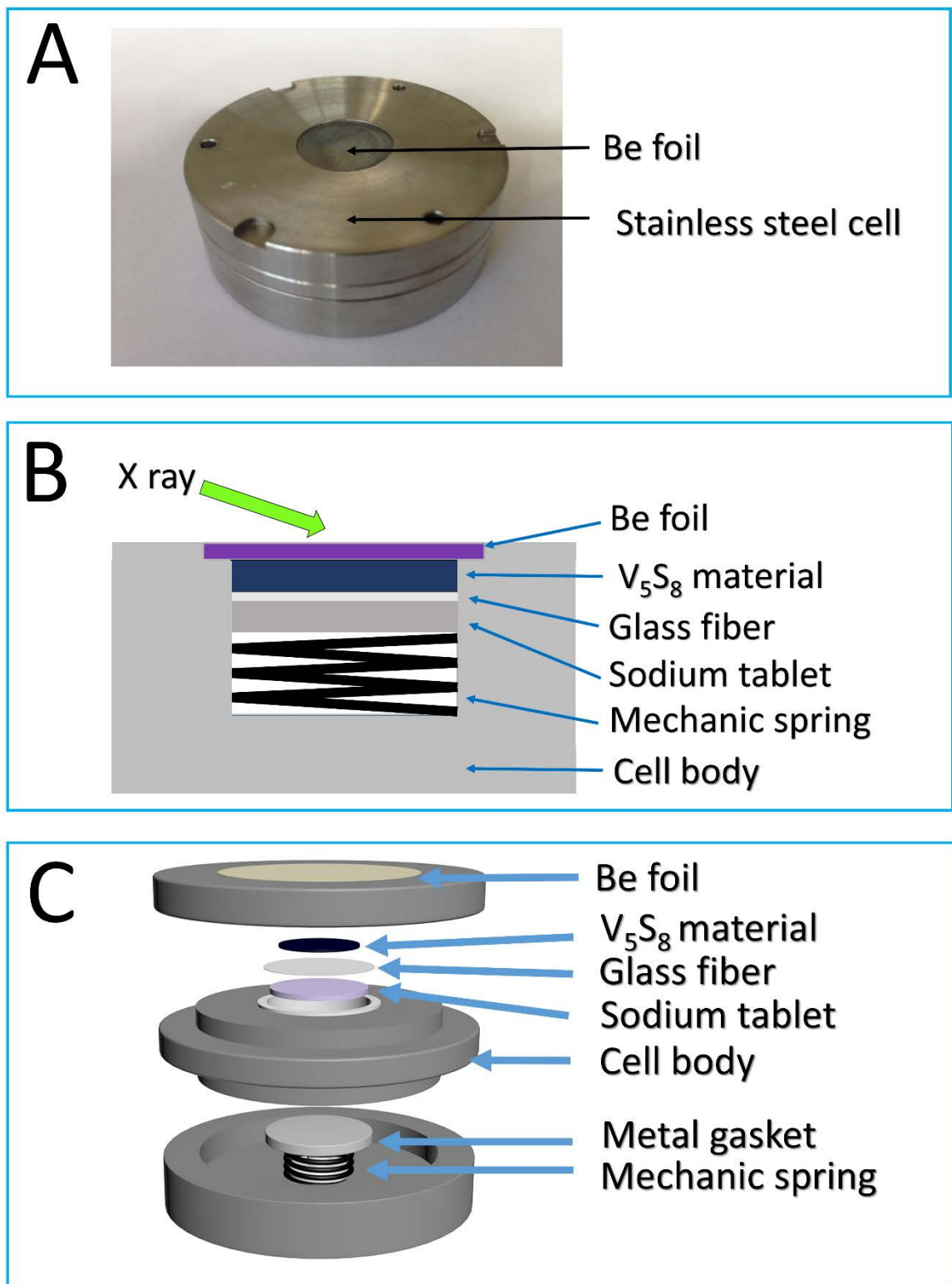


Fig. S4 Photograph (A) and assembly drawing of the *in situ* XRD cell utilized for the *in situ* XRD measurements (B and C).

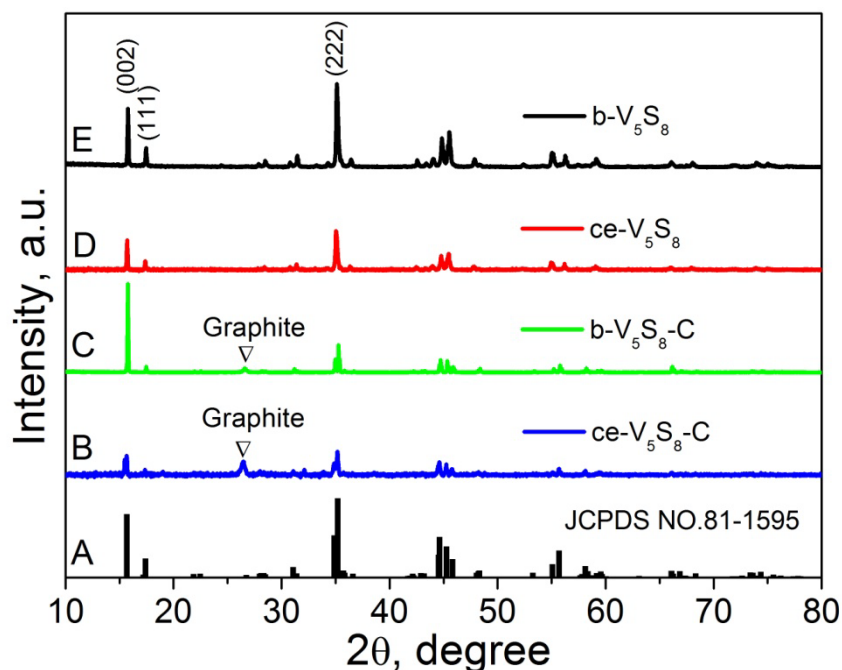


Fig. S5 XRD patterns of b- V_5S_8 , bulk V_5S_8 -graphite (b- V_5S_8 -C), chemically exfoliated V_5S_8 (ce- V_5S_8) and chemically exfoliated V_5S_8 -graphite (ce- V_5S_8 -C), respectively.

XRD patterns of V_5S_8 and V_5S_8 -C before and after chemical exfoliation are shown in Fig. S5. The diffraction peaks of pristine b- V_5S_8 and b- V_5S_8 -C hybrids agree well with the monoclinic structured V_5S_8 (JCPDS: 81-1596, space group $F2/m(12)$). The primary (002) diffraction peak centered at 15.7° in the XRD patterns indicates that the layered V_5S_8 is preferentially grown along the c -axis. The diffraction peaks of ce- V_5S_8 and ce- V_5S_8 -C samples remain almost identical, implying that the layered structure did not change during the chemical exfoliation. However, compared with the pristine b- V_5S_8 -C, the (002) peaks of ce- V_5S_8 and ce- V_5S_8 -C samples are broadened with markedly reduced intensity, signaling formation of ultrathin V_5S_8 sheets.^{S3,S4} Moreover, a small peak at 26.3° observed relates to the (002) plane of graphite, confirming the presence of graphite.

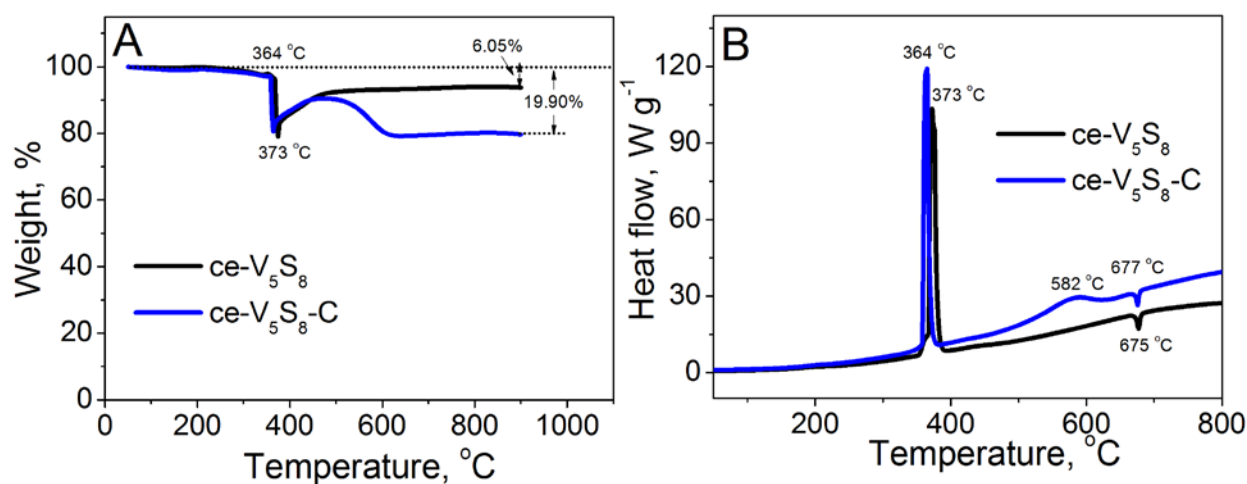


Fig. S6 TGA (A) and DSC (B) curves of ce-V₅S₈ nanosheets and ce-V₅S₈-C nanosheets.

To quantify the amount of graphite in ce-V₅S₈-C nanosheets, TGA-DSC measurements for the ce-V₅S₈-C nanosheets and ce-V₅S₈ nanosheets were carried out in air from 50 to 800 °C at a rate of 10 °C min⁻¹, as shown in Fig. S6. For the ce-V₅S₈ nanosheets, an exothermal peak located at 364 °C is clearly observed in the DCS curve, and it is accompanied with an abruptly weight loss in the TGA curve, suggesting the oxidation of V₅S₈ and generation of V₂O₅. After the phase transformation, the weight loss is calculated to be about 6.05 wt.%. However, an additional exothermal peak has been observed in the DCS curve of ce-V₅S₈-C nanosheets at around 582 °C, accompanied with incessant weight loss for TGA test, which is related to the thermal decomposition and oxidation of graphite. The weight loss of ce-V₅S₈-C nanosheets is estimated to be 19.90 wt.%. Therefore, the graphite content in ce-V₅S₈-C nanosheets calculated based on the TGA-DSC analysis is 14.74 wt.%.

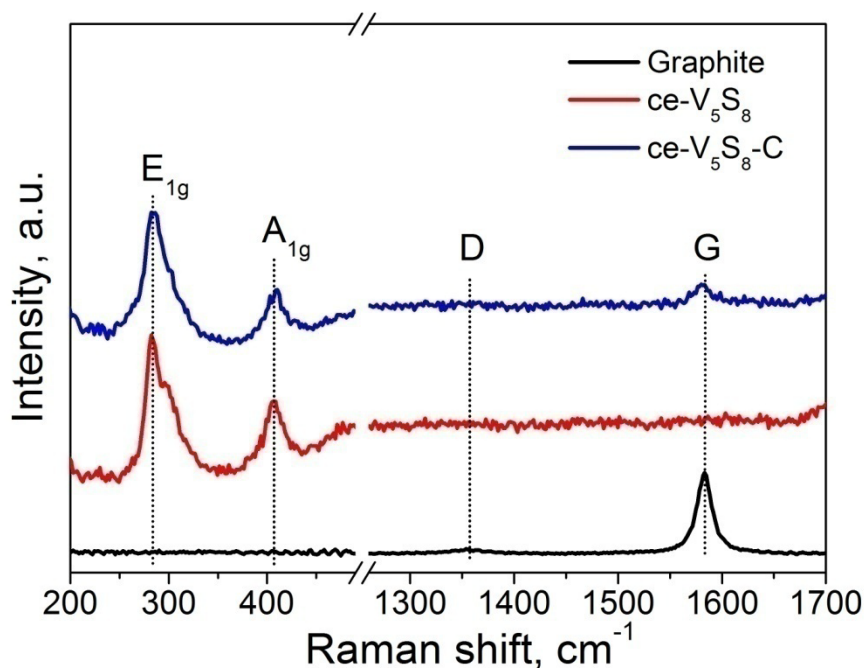


Fig. S7 Raman spectra of pristine graphite, ce-V₅S₈ and ce-V₅S₈-C.

Fig. S7 shows the Raman spectra of ce-V₅S₈-C nanosheets, ce-V₅S₈ nanosheets and graphite. The spectrum of ce-V₅S₈-C is virtually a mixture of V₅S₈ and graphite. The two peaks in the wave number range between 300 and 500 cm⁻¹ correspond to hexagonal V₅S₈. The peak centered at 282 cm⁻¹ is related to E_{1g} of hexagonal VS₂ caused by a curvature, and A_{1g} peak centered at 406 cm⁻¹ is associated with the opposite vibration of two S atoms with respect to V atom.^{S5, S6} The two peaks around 1353 cm⁻¹ (very weak) and 1583 cm⁻¹ observed in ce-V₅S₈-C nanosheets are very similar to the pure graphite (except intensity), which are attributed to D-band and G-band of graphite arise from defect/disorder in the hexagonal graphitic layers and vibration of sp² carbon atoms with a type of 2D hexagonal lattice, respectively. It confirms the existence of graphite in ce-V₅S₈-C nanosheets.^{S7}

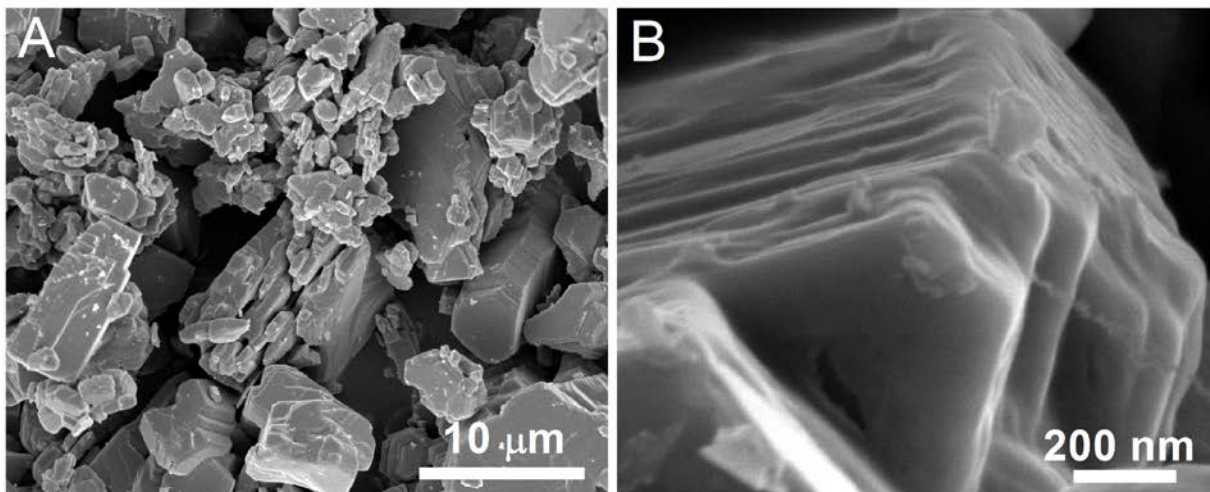


Fig. S8 SEM images of b-V₅S₈ materials.

The morphology of b-V₅S₈ is shown in Fig. S8, it has a typical layered structure, and thickness of the b-V₅S₈ flakes is about 2-3 μm.

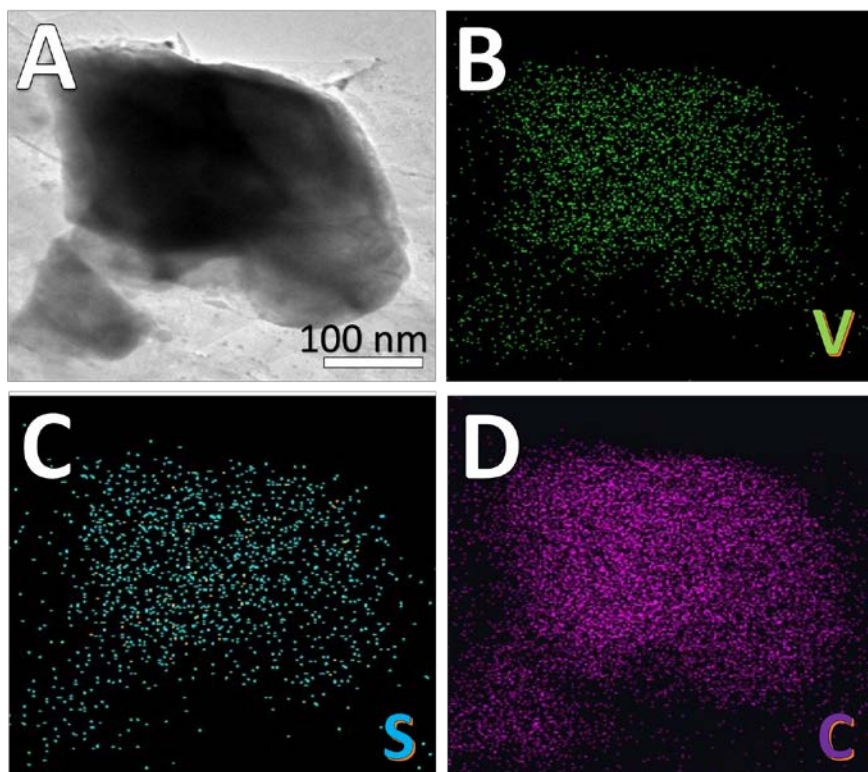


Fig. S9 SEM images of ce- V_5S_8 -C nanosheets (A), and the corresponding EDX elemental mapping images of V (B), S (C) and C (D).

Fig. S9 shows the SEM images of the ce- V_5S_8 -C nanosheet and the corresponding EDX elemental mapping images of V, S and C. It reveals that the V, S and C are homogeneously distributed in the ce- V_5S_8 -C nanosheet, indicating graphite is uniformly coated on the ce- V_5S_8 nanosheets.

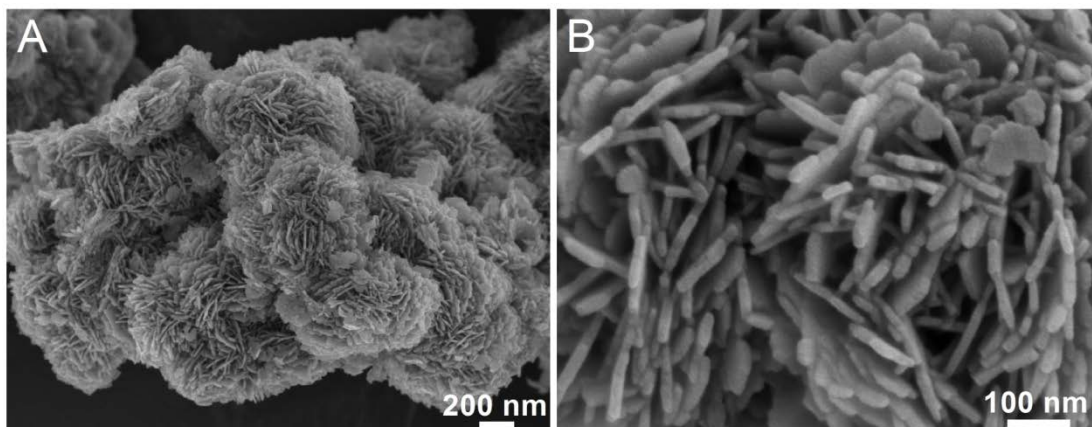


Fig. S10 SEM images of ce-VS₂ nanosheets prepared by the chemical exfoliation method.

The SEM images of chemically exfoliated VS₂ (ce-VS₂) are shown in Fig. S10. It can be seen that the ce-VS₂ sample exhibits a flower like morphology (Fig. S10A). Fig. S10B shows a magnified SEM image of ce-VS₂ microflowers, which is consisted of VS₂ nanosheets. The thickness of ce-VS₂ nanosheets is about 10-15 nm.

Table S1. Electrochemical performance comparison of the as-prepared ce-V₅S₈-C based anode with previously reported TMDs based anodes.

Materials	Current density, mA g ⁻¹	Cycling capacity, mAh g ⁻¹ (cycle number, n)		Rate capacity, mAh g ⁻¹ (current density, A g ⁻¹)			Material loading, mg	Areal capacity, mAh cm ⁻²	Electrode density, mg cm ⁻²	Electrode composition *	Ref.
FeS ₂	40	530(1)	415(100)	480(0.08)	400(0.1)	290(0.2)	---	---	1.5	8.5:1:0.5	34
TiS ₂	480	187(1)	142(300)	143(2)	121(5)	101(10)	---	---	---	8:1:1	35
NbS ₂	500	170(2)	157(100)	137(1)	106(2)	93(5)	1.13	177	1	7:2:1	36
WS ₂ -rGO	200	400(1)	334(200)	404(0.1)	330(0.5)	287(0.9)	1.4	400	1.4	7:2:1	37
NiS ₂ -rGO	100	407(5)	314(200)	278(0.5)	221(1)	169(2)	---	---	---	7:2:1	38
MoS ₂ -graphene	100	386(1)	313(200)	302(1)	280(2)	247(5)	3	491	3.8	8:1:1	39
MoS ₂ -rGO	1500	385(1)	323(600)	427(1)	306(5)	234(10)	1.2	385	1.2	7:1.5:1.5	40
VS ₄ -rGO	100	360(1)	240(50)	267(0.3)	219(0.5)	192(0.8)	1.2	---	---	7:2:1	41
ZnS	640	580(1)	423(100)	480(0.16)	465(0.3 2)	423(0.6 4)	1.2	---	---	8:1:1	42
Cu ₂ NiSnS ₄	50	631(1)	321(100)	118(2)	49(5)	14(5)	1.02	558	0.91	7:2:1	43
CoS-C NW	100	381(2)	294(100)	316(0.5)	285(2)	165(5)	---	485	---	9:1:0	44
CoSe-C NW	100	344(2)	299(100)	308(0.5)	268(2)	241(5)	---	438	---	9:1:0	44
MoSe ₂ -CNT	1000	350(5)	296(250)	310(1.5)	280(3)	255(5)	1.2	350	1.2	7:2:1	45
WSe ₂ -C	200	467(1)	270(50)	240(0.5)	230(0.8)	208(1)	0.79	595	1.0	8:1:1	46
CoSe _r -rGO	300	525(2)	420(50)	389(0.6)	375(0.8)	357(1)	1.2	525	1.2	7:2:1	47
NiSe ₂ -rGO	200	540(1)	480(100)	313(1)	269(2)	243(3)	2.25	240	1.2	7:2:1	48
FeV ₂ S ₄	75	596(2)	529(10)	550(0.075)	500(0.1 5)	350(0.3 75)	3.0	759	3.82	8:1:1	49
ce-V₅S₈-C	1000	616(1)	488(500)	485(2)	389(5)	344(10)	1.18	545	1.05	7:2:1	This work

* : The list of electrode composition ratio contain the active material, the conductive material and the binder.

---: The relevant data is not mentioned in the article.

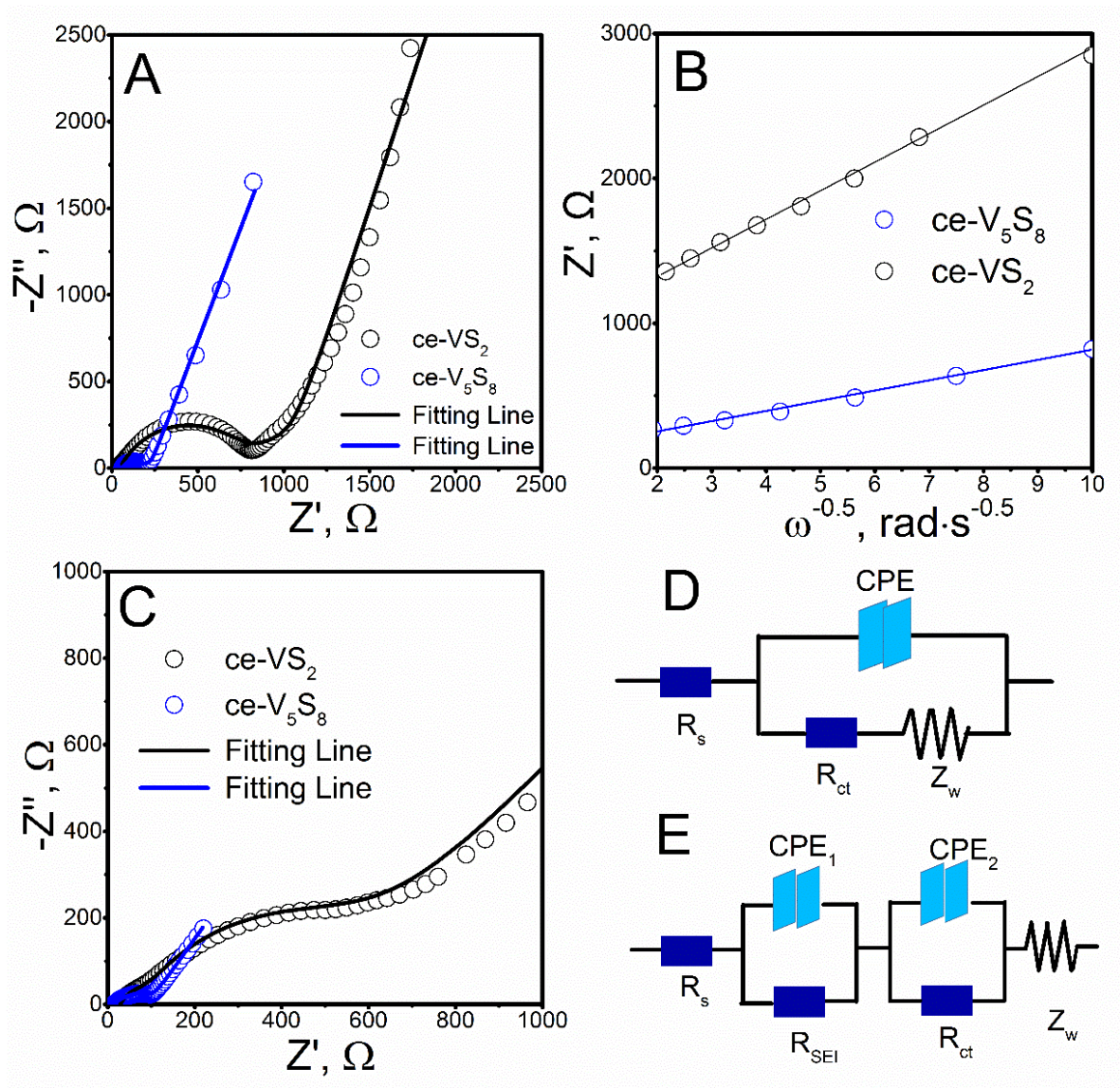


Fig. S11 Nyquist plots of ce-VS₂ and ce-V₅S₈ nanosheets as the anode materials for SIBs before (A) and after (C) 100 cycles test under 1.0 A g⁻¹. The linear fits of the Z' vs $\omega^{-1/2}$ curves of samples before cycling (B), and the equivalent circuit models for before (D) and after cycling (E).

Table S2. Impedance parameters derived using equivalent circuit model (Fig. S11D and Fig. 11E) for ce-VS₂ and ce-V₅S₈ nanosheets as the anode materials for SIBs before (Fig. 11A) and after (Fig. 11C) 100 cycles test under 1.0 A g⁻¹, respectively.

Sample	Before cycling				After cycling		
	R _s , Ω	R _{ct} , Ω	σ, S ⁻¹ s ^{-0.5}	D _{Na} , cm ² s ⁻¹	R _s , Ω	R _{SEI} , Ω	R _{ct} , Ω
ce-VS ₂	42.8	692.1	68.5	5.01 × 10 ⁻¹³	28.8	46.2	472.1
ce-V ₅ S ₈	52.3	160.7	189.9	3.84 × 10 ⁻¹²	30.1	12.8	70.5

Fig. S11A shows that both of the electrochemical impedance spectra (EIS) profiles of ce-V₅S₈ and ce-VS₂ exhibited a semicircle in the high-frequency region and a straight line in the low-frequency region. The Nyquist plots were further simulated by a simplified equivalent circuit shown in Fig. S11D. The depressed semicircle in the high-frequency region is related to the charge transfer resistance (R_{ct}) of electrode reaction at the electrode-electrolyte interface. While, the inclined line in the low-frequency range represents the Warburg impedance (W) associated with Na⁺ diffusion through ce-V₅S₈. The Na⁺ ions diffusion coefficient (D_{Na}) of ce-V₅S₈ anode can be determined by the following equations (1-2),^{46,S8,S9}

$$D_{\text{Na}} = \frac{R^2 T^2}{2A^2 n^4 F^4 C_{\text{Na}}^2 \sigma^2} \quad (1)$$

where R is the universal gas constant, A is the active anode surface area, n is the number of transferred electrons, F is the Faraday's constant, C is the concentration of Na⁺ ions in the cathode electrode and T is the absolute temperature, σ is the Warburg factor associated with Z',

$$Z' = R_s + R_{ct} + \sigma \omega^{-0.5} \quad (2)$$

where R_s represents the ohmic resistance mainly from the electrolyte and separator, ω is the angular frequency in the low-frequency Warburg region. The plot of Z' against ω^{-0.5} in the low-frequency region is a straight line with the slope of σ. The fitting results are shown in Table S2. R_{ct} of ce-V₅S₈ is 160.7 Ω, which is much smaller than that of ce-VS₂ for 692.1 Ω. Moreover,

the value of D_{Na} in ce- V_5S_8 ($3.84 \times 10^{-12} \text{ cm}^2 \text{ s}^{-1}$) is nearly one order of magnitude higher than that of ce- VS_2 ($5.01 \times 10^{-13} \text{ cm}^2 \text{ s}^{-1}$), indicating enhanced diffusion of sodium ions in the ce- V_5S_8 . After 100 cycles at 1.0 A g^{-1} , the R_{ct} of ce- V_5S_8 is still much smaller than that of ce- VS_2 (Table S2), which is consistent with previous cycling stability testing results (Fig. 3F). These results confirm that the intrinsic high electronic and ionic conductivities of ce- V_5S_8 resulting from its unique structure in comparison with ce- VS_2 (Fig. 1) can greatly enhance the electrons and Na^+ ions transport during the insertion/extraction reaction and therefore achieve a significantly improved electrochemical performance. Meanwhile, as illustrated in Fig. S12 and Table S3, the ce- V_5S_8 -C composite show a further reduced R_{ct} of $64.3 \ \Omega$. Based on the above results, it is concluded that the incorporation of graphite in ce- V_5S_8 -C can further improve the electronic conductivity of ce- V_5S_8 nanosheets and facilitate the Na^+ transport, especially, at the high current rate when the Na^+ transport is rate limiting between ce- V_5S_8 -C anode and electrolyte.

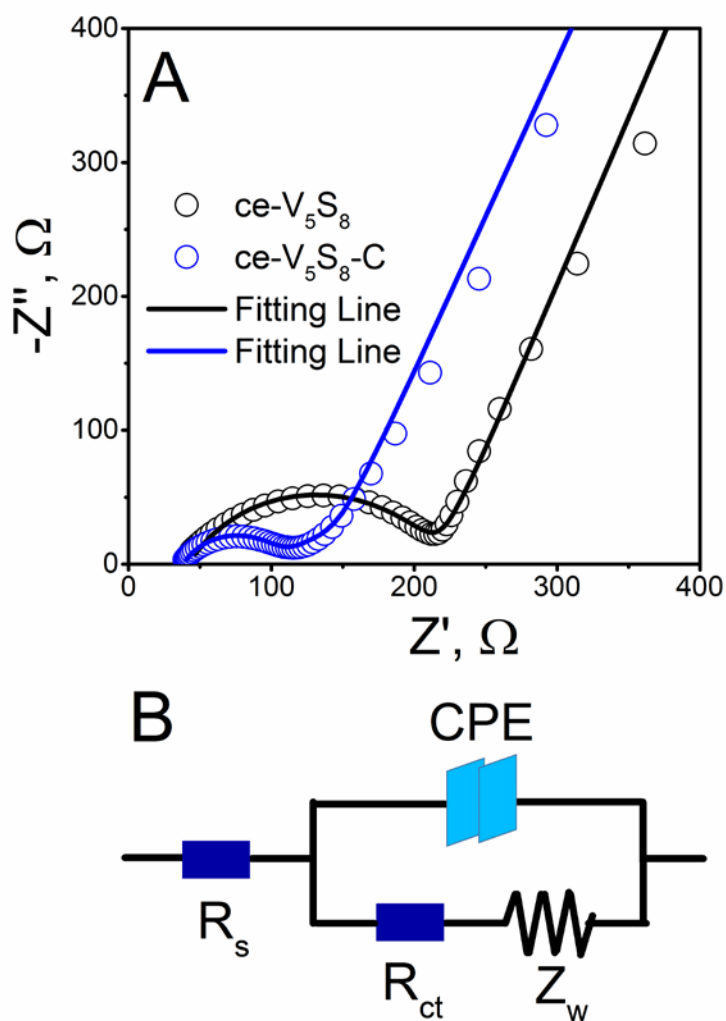


Fig. S12 Nyquist plots of the ce-V₅S₈ and ce-V₅S₈-C as the anode materials for SIBs before cycling (A), and the equivalent circuit model (B).

Table S3. Impedance parameters derived using equivalent circuit model (Fig. S12B) for ce-V₅S₈ and ce-V₅S₈-C nanosheets as the anode materials for SIBs before cycling, respectively.

Samples	R _s , Ω	R _{ct} , Ω
ce-V ₅ S ₈	52.3	160.7
ce-V ₅ S ₈ -C	49.7	64.3

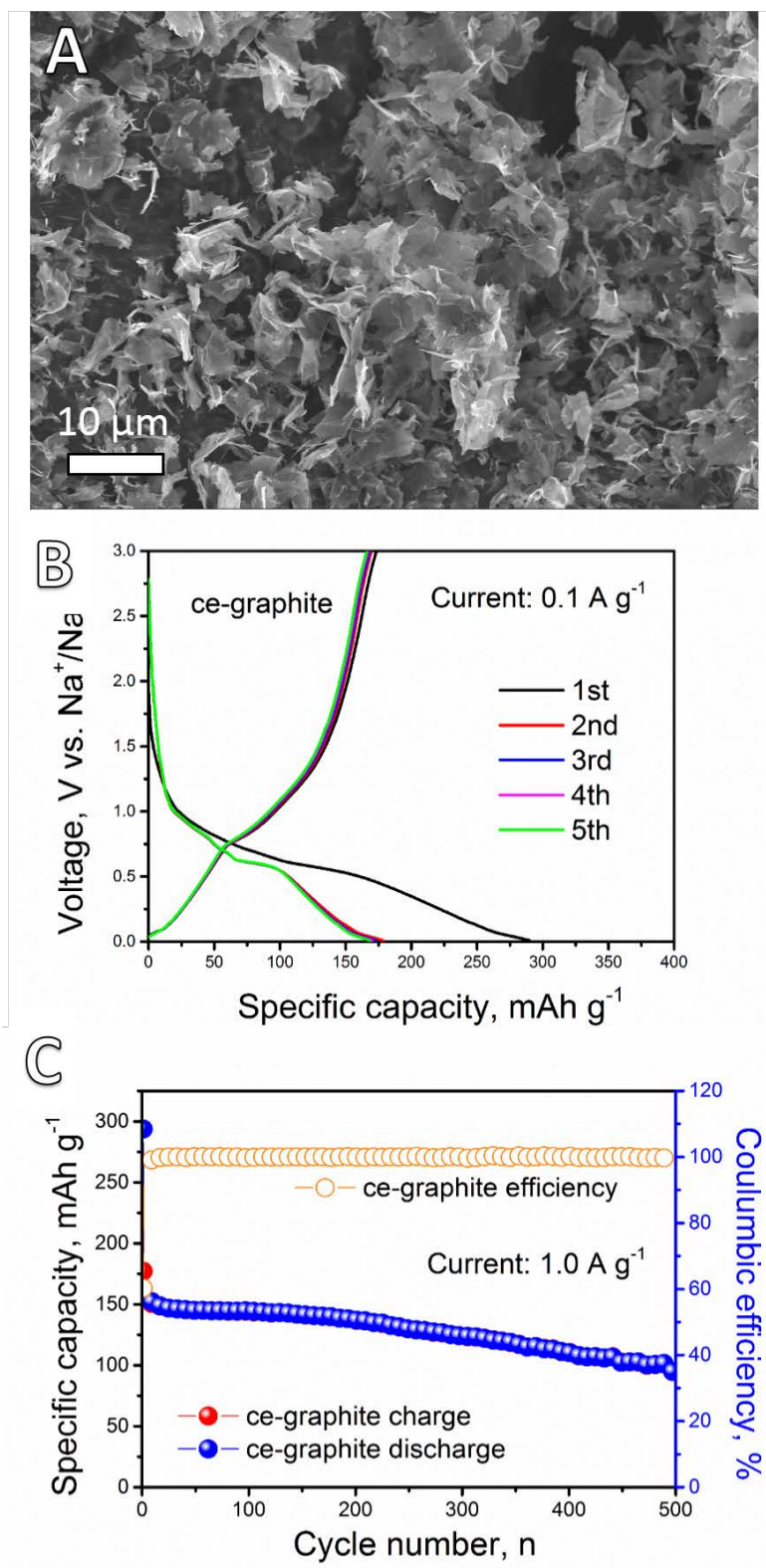


Fig. S13 SEM images of (A), first five-cycle charge-discharge profiles at 0.1 A g^{-1} (B), cycling performance at 1.0 A g^{-1} (C) of pure graphite prepared by the chemical exfoliation method (ce-graphite) as the anode materials for SIBs.

The SEM images and electrochemical performance of pure graphite prepared by the chemical exfoliation method (ce-graphite) as the anode materials of SIBs are shown in Fig. S13A. It is shown that the ce-graphite consists of flake-like nanosheets. Fig. S13B further shows the initial five-cycle galvanostatic charge/discharge profiles of ce-graphite at 0.1 A g⁻¹. The ce-graphite exhibits discharge and charge capacities of 289.8 and 173.4 mAh g⁻¹ in the first cycle, respectively, with a Coulombic efficiency of 59.83%. In the second cycle, it delivers discharge and charge capacities of 178.2 and 169.6 mAh g⁻¹, respectively. From the second cycle onwards, the charge/discharge profiles are almost unchanged. When cycled at 1.0 A g⁻¹ for long-term (Fig. S13C), the ce-graphite delivers an initial reversible capacity of 156.5 mAh g⁻¹, while it still retains a reversible capacity of 98.8 mAh g⁻¹, corresponding to 63.1% of its initial discharge capacity, after 500 cycles.

The specific capacity and long-term stability of ce-V₅S₈ are much better than that of ce-graphite as indicated in Fig. 3A and 3G. After coated with amorphous graphite forming ce-V₅S₈-C hybrid, the initial discharge capacity of ce-V₅S₈-C is increased to 902 mAh g⁻¹ at 0.1 A g⁻¹ (Fig. 3B). The rate capacity (Fig. 3E) and cycling stability (Fig. 3G) of the ce-V₅S₈-C are also enhanced by the presence of graphite.

Overall, the graphite-enhanced performance arises from the improved electronic conductivity, enhanced cation diffusion efficiency, suppressed volume expansion, formation of a stable SEI and stabilization of electrode microstructure.

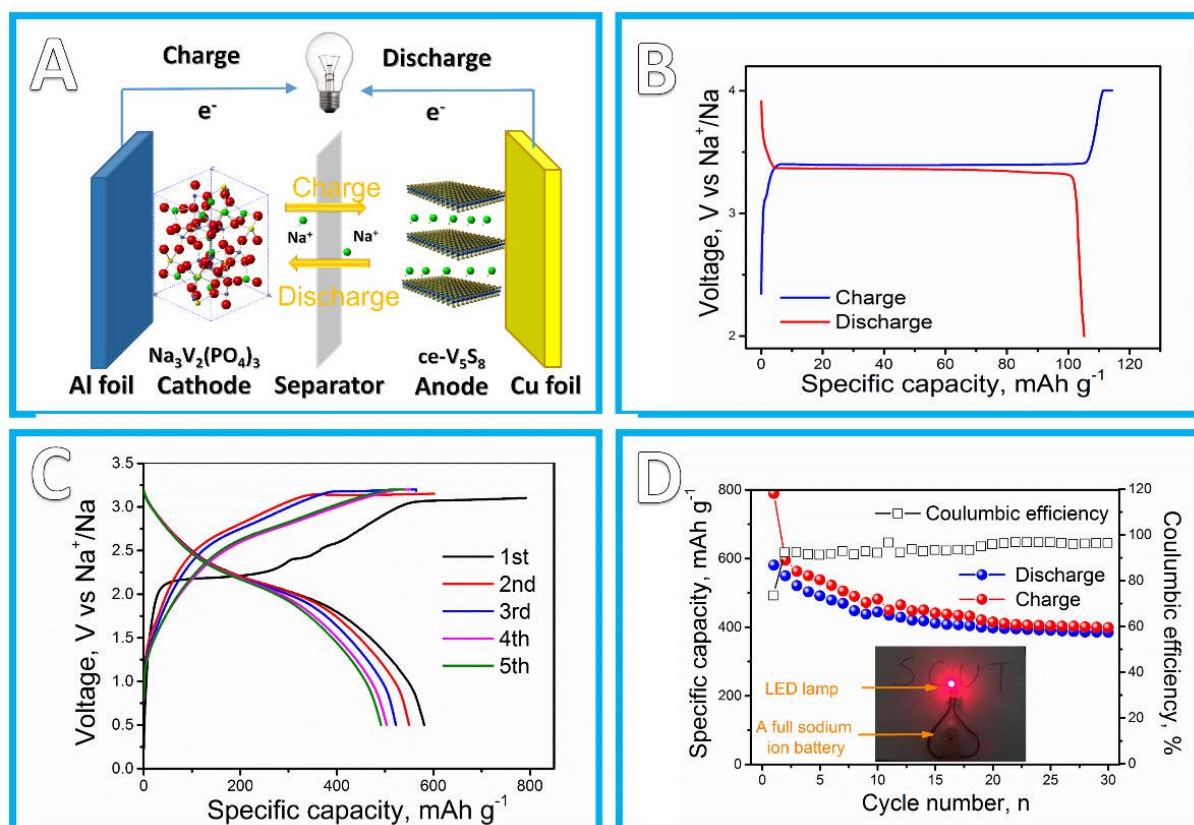


Fig. S14 (A) Illustration of Na₃V₂(PO₄)₃/ce-V₅S₈-C full SIB; (B) the charge/discharge profile of Na₃V₂(PO₄)₃ cathode at 0.02 A g⁻¹ from 2.0 to 4.0 V with Na anode; (C) the first five-cycle charge/discharge profiles at 0.2 A g⁻¹ from 0.5 to 3.2 V of a full SIB with the ce-V₅S₈-C as anode and Na₃V₂(PO₄)₃ as cathode, respectively; (D) the corresponding cycling performance of Fig. S14 (D).

For the full battery, the specific capacity of cathode was calculated based on the total mass of the Na₃V₂(PO₄)₃ cathode, which was controlled at 7.7 mg. Meanwhile, the mass loading of ce-V₅S₈-C anode was still 0.77 mg with 0.655 mg ce-V₅S₈ and 0.115 mg ce-graphite.

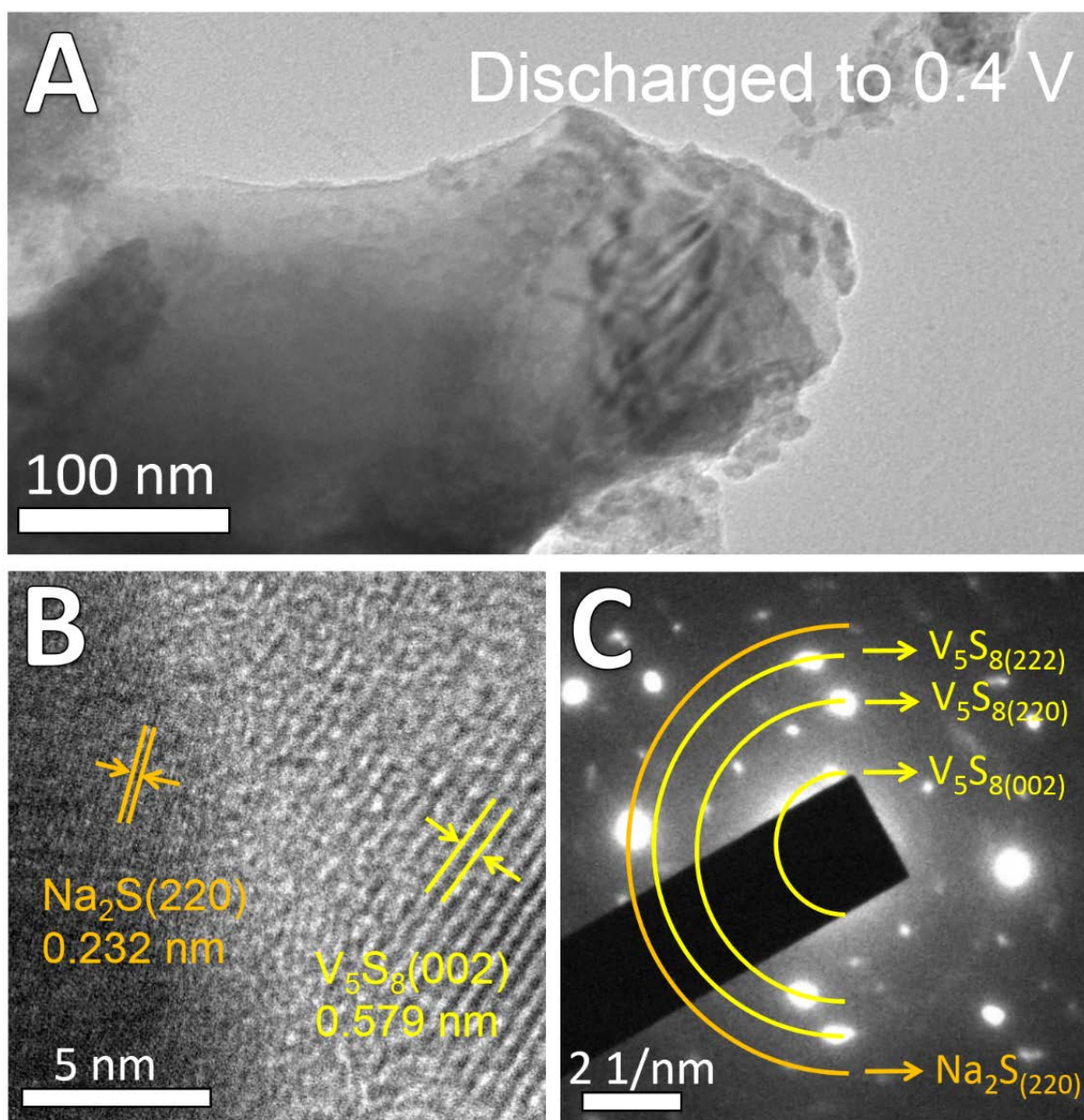


Fig. S15 *Ex situ* TEM (A), HRTEM (B) images and SAED pattern (C) of ce-V₅S₈-C hybrid anode after discharged to 0.4 V.

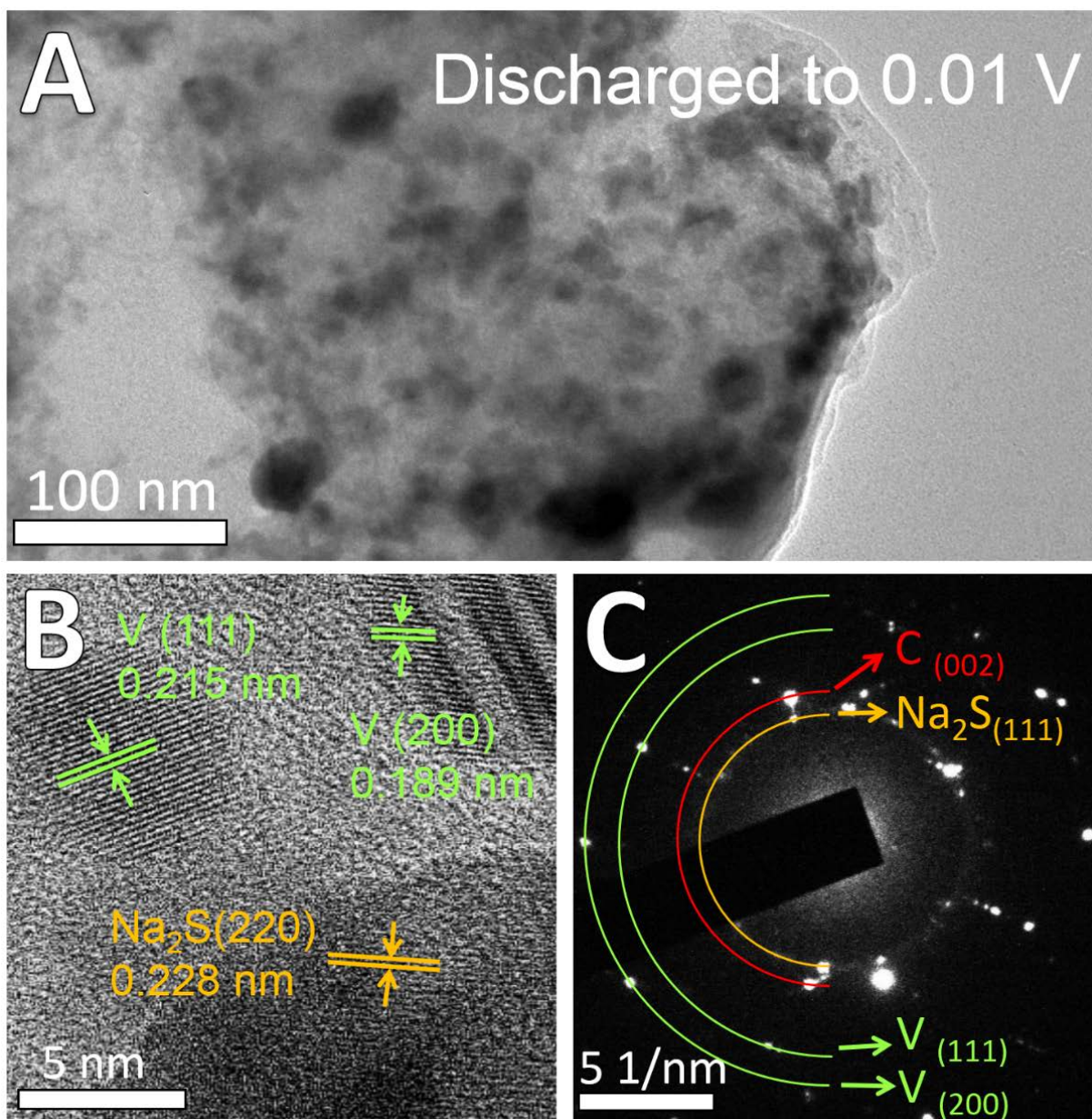


Fig. S16 *Ex situ* TEM (A), HRTEM (B) images and SAED pattern (C) of ce-V₅S₈-C hybrid anode after discharged to 0.01 V.

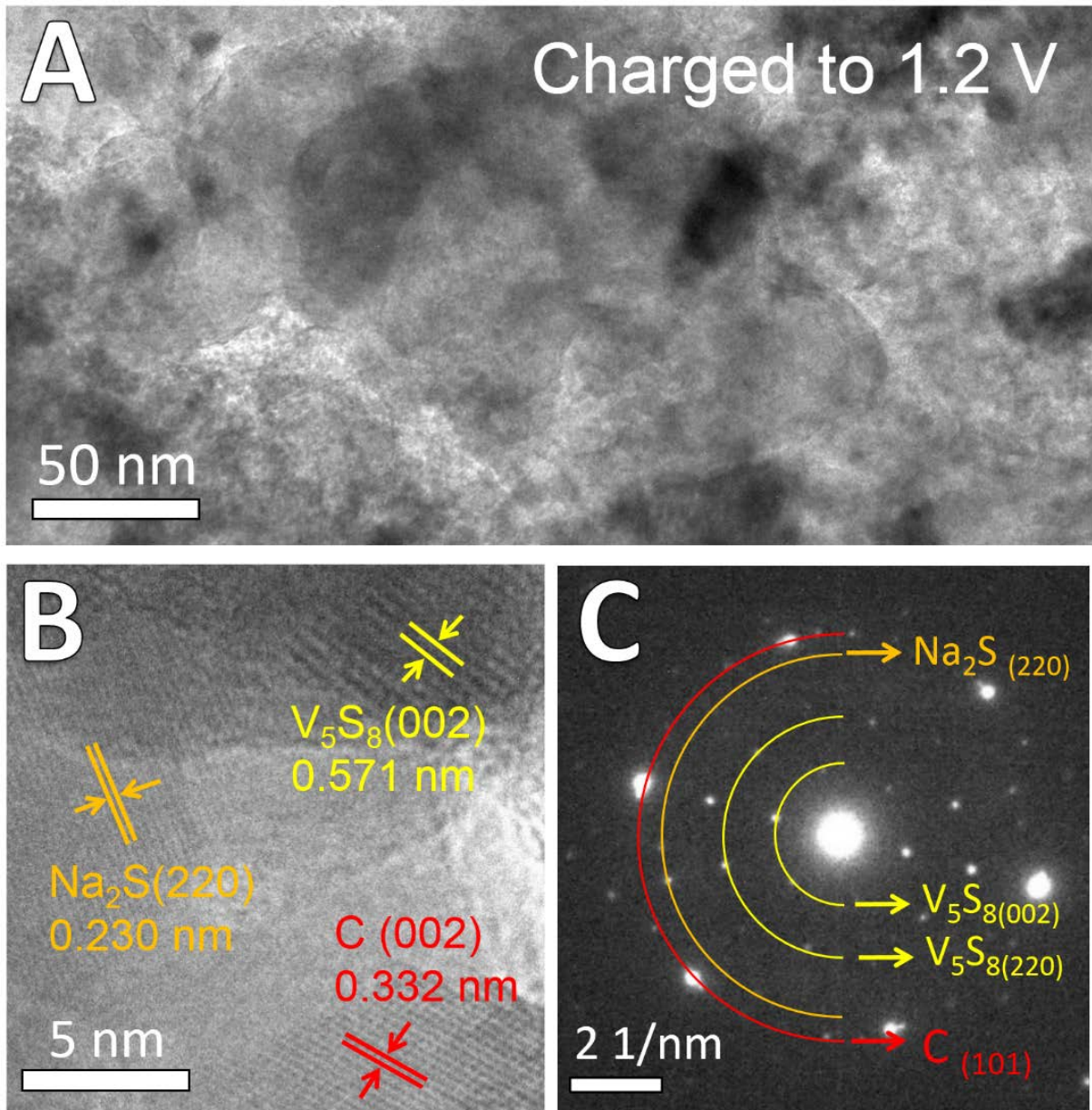


Fig. S17 *Ex situ* TEM (A), HRTEM (B) images and SAED pattern (C) of ce-V₅S₈-C hybrid anode after charged to 1.2 V.

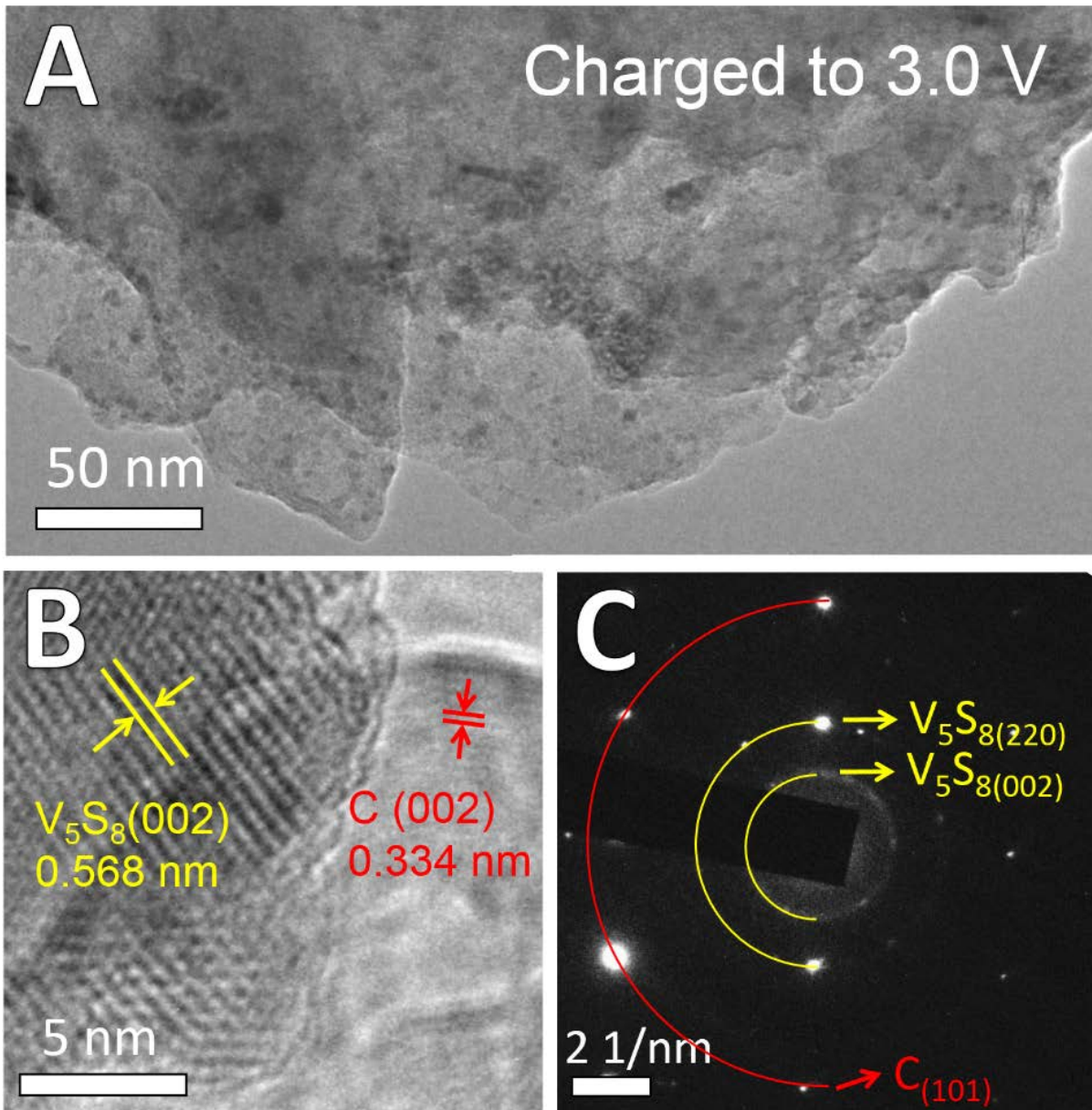


Fig. S18 *Ex situ* TEM (A), HRTEM (B) images and SAED pattern (C) of ce- V_5S_8 -C hybrid anode after charged to 3.0 V.

To confirm the *in situ* XRD results and clarify the mechanisms for reversible sodiation/desodiation in the ce- V_5S_8 -C hybrid anode, we performed *ex situ* TEM to analyze the microstructure of the ce- V_5S_8 -C anode after operated at different charge/ discharge states. The observations are summarized below:

- When discharged to 0.4 V, Fig. 15 B shows that the interplanar spacing at 0.579 nm in the anode can be indexed to V_5S_8 (002), while that at 0.232 nm can be indexed to Na_2S

((220), JCPDS 77-2149). Note that the interplanar spacing of V_5S_8 (002) is slightly larger than that of the original V_5S_8 (002) (compare Fig. 2E and F); this is an indication of Na^+ -ion intercalation into the V_5S_8 nanosheets, forming $Na_xV_5S_8$. The SAED patterns shown in Fig. S15C are also in good agreement with the HRTEM results.

- When discharged to 0.01 V, a fully sodiated state, Fig. S16A shows that some nanoparticles (10-30 nm) are embedded in the porous matrix. The interplanar spacings of the nanoparticles are 0.189 and 0.215 nm, corresponding to (111) and (200) plane of metal V (JCPDS 88-2322), respectively. Fig. S16B further shows that the matrix has an interplanar spacing of 0.228 nm, corresponding to the (220) plane of Na_2S .
- When recharged to 1.2 V, Fig. 17B shows that the interplanar spacings in the anode are 0.228 nm, which is related to the (220) plane of Na_2S , and 0.571 nm, which is closely related to the (002) plane of V_5S_8 , respectively.
- When fully recharged to 3.0 V, Fig. S18B shows that interplanar spacing of 0.568 nm closely related to the (002) plane of V_5S_8 still remains visible. This observation is a critical evidence for the formation of V_5S_8 and reversibility of the recharging process.

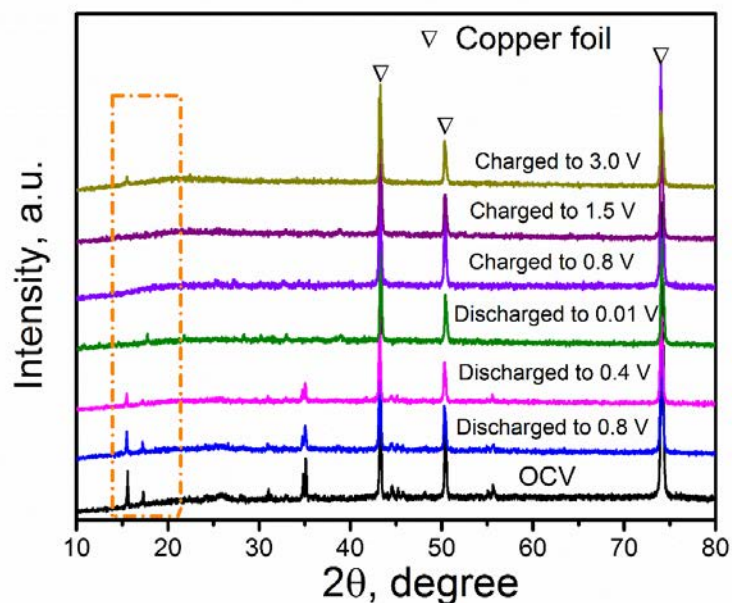


Fig. S19 *Ex situ* XRD results at different discharge/charge states of ce- V_5S_8 -C hybrid anodes.

The *ex situ* XRD patterns of the ce- V_5S_8 -C hybrid anodes at selected charge/discharge states shown in Fig. S19. The peaks located at 43.3° , 50.4° and 74.1° are derived from copper foil. The findings are summarized below:

- When discharged from OCV to 0.4V, the peaks of V_5S_8 can be observed at 15.7° , 17.4° and 35.2° that gradually shift to low 2θ , suggesting a lattice expansion of ce- V_5S_8 nanosheets caused by Na^+ intercalation.
- When fully discharged to 0.01 V, the peaks of V_5S_8 disappeared, while a new peak located at 38.9° assigned to the characteristic peak of Na_2S is observed, indicating the occurrence of conversion reaction.
- When recharged to 3.0 V, V_5S_8 phase is detected at 15.7° , indicating the reappearance of V_5S_8 at fully charged state. These results are also well consistent with the *in situ* XRD test results shown in the main context.

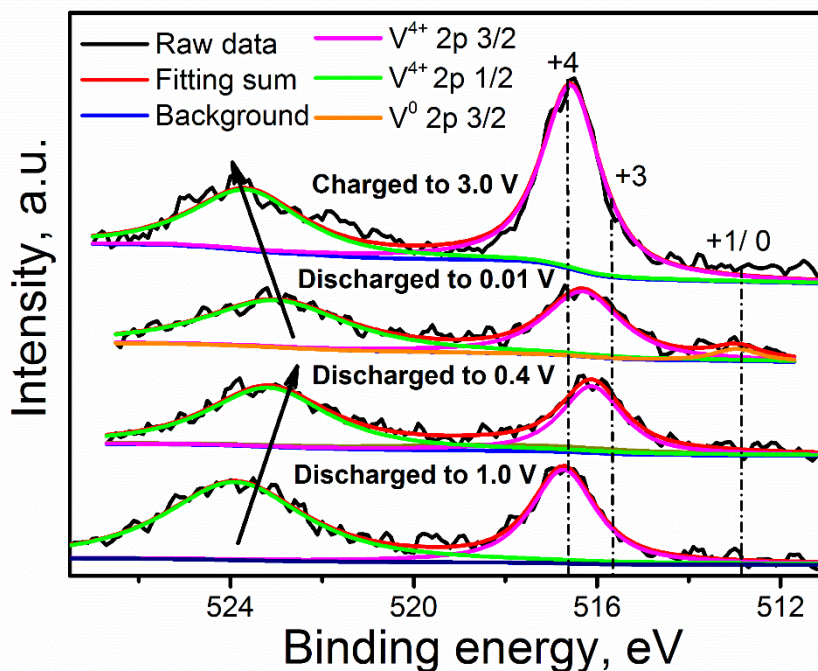


Fig. S20 *Ex situ* XPS results at different discharge/charge states of ce- V_5S_8 -C hybrid anodes.

To further understand the charge/discharge process of ce- V_5S_8 -C hybrid anodes, the evolution of V oxidation-state at selected charged states during the first sodiation-desodiation process was investigated by XPS; the results are shown in Fig. S20 and summarized below:

- The XPS peaks of V-2p oxidation state can be deconvoluted into two subsets at 524.1 and 516.8 eV, respectively. As depicted in the figure, the binding energies of V-2p shifted gradually to lower value during the discharge process, an indicative of a change in the oxidation state of V.
- When discharged to 0.01 V, the peaks at 515.7 and 523.0 eV are assigned to V^{3+} , while the peak located at 512.8 eV is assigned to the V^0 , suggesting that V^{4+} is firstly reduced into V^{3+} and then to metal V during the discharge process.
- When charged to 3.0 V, the peaks shift to high binding energy and the V oxidation state resumes to V^{4+} , indicating the V_5S_8 are formed at a fully charged state. Therefore, it comes to the conclusion that the ce- V_5S_8 -C hybrid anode demonstrates reversible charge/discharge process.

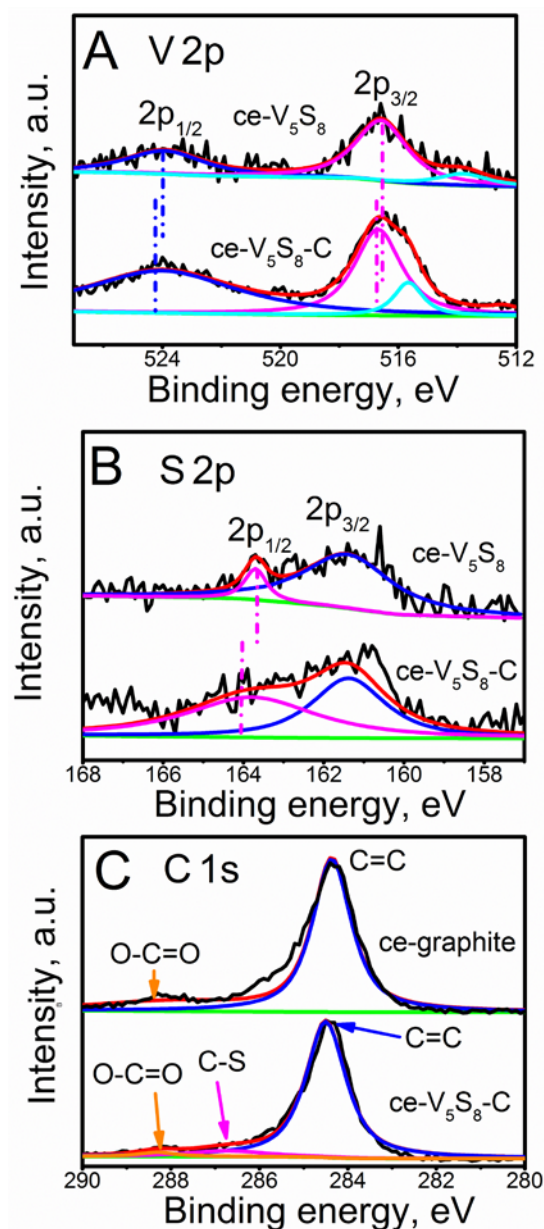


Fig. S21 XPS spectra of V-2p (A), S-2p (B) and C-1s (C) core level of ce-V₅S₈, ce-V₅S₈-C and graphite, respectively.

To confirm chemically the presence of C layer on the surface of V₅S₈ nanosheets, we performed x-ray photoelectron spectroscopy (XPS) on ce-V₅S₈, ce-V₅S₈-C and graphite. The V-2P, S-2p and C-1S core levels XPS spectra of ce-V₅S₈, ce-V₅S₈-C and graphite samples are shown in **Fig. S21**, respectively. The binding energy for V-2p_{3/2} and V-2p_{1/2} are located at 516.5 and 523.9 eV (Fig. S21A), showing the existence of V⁴⁺ in ce-V₅S₈. Moreover, a tiny peak of V-2p_{3/2} located at 513.8 eV is also observed, which is ascribed to the V³⁺ or V.^{S11,S12}

The binding energies of S-2p_{3/2} and S-2p_{1/2} located at 161.2 and 163.8 eV (Fig. S21B) suggest the existence of S²⁻ in ce-V₅S₈. The C-1s peak located at 284.8 eV is ascribed to the sp² C-C in ce-graphite (Fig. S21C).^{S13}

For the ce-V₅S₈-C, the characteristic peaks of V and S (see Fig. S21A and B) shift towards higher binding energy, suggesting an increased density of electron clouds around the ce-V₅S₈ nanosheets. Meanwhile, the peak associated with C=C is narrowed, and an additional peak related to the C-S bond appears at 266.5 eV, reflecting increased bonding energy between C and ce-V₅S₈. The XPS results clearly indicate that there is a strong electron interaction between V₅S₈ nanosheets and the C layer overcoated, which are expected to allow ce-V₅S₈-C to maintain a stable structure for long-term cycling in SIBs.^{S14,S15}

We have also performed another HRTEM study on ce-V₅S₈-C sample to provide new microscopic evidence to the existence of C layer on the surface of ce-V₅S₈. Fig. S22 shows a HRTEM image capturing the regions of C-layer and V₅S₈ layer with respective interplanar spacings.

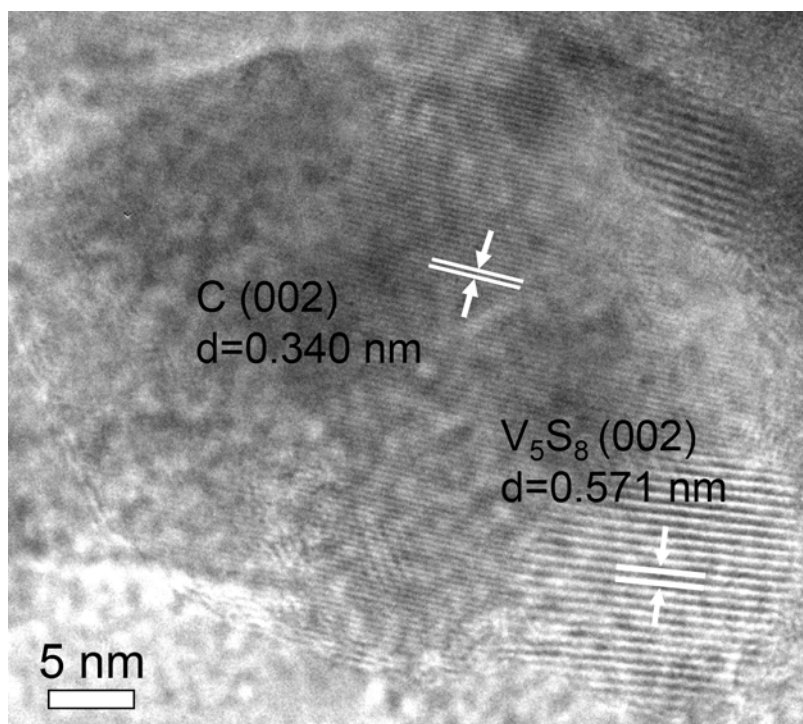


Fig. S22 A HRTEM image of ce-V₅S₈-C nanosheets.

Table S4. The loss of sulfur species for the ce-V₅S₈ and ce-V₅S₈-C at various states in a voltage window 0.01-3.0 V vs in the first cycle. The content of Na/Na⁺ was analyzed by ICP based on element weight in the electrodes.

Samples	Amount of sulfur dissolved, wt.%		
	Discharged to 0.2 V	Discharged to 0.01 V	Charged to 3.0 V
ce-V ₅ S ₈	2.33	4.95	1.36
ce-V ₅ S ₈ -C	1.29	2.05	0.95

In order to determine loss of sulfur species (sulfur and polysulfide due to dissolution into electrolyte) during the sodiation/desodiation process, we performed ICP (Inductive Coupled Plasma Emission Spectrometer) analysis on a fully sodiated anode. The ICP results are given in Table S4. For the ce-V₅S₈ anode, the loss of sulfur species is 4.95 wt.% when it is discharge to 0.01 V. However, for the ce-V₅S₈-C anode, the loss of sulfur species S is 2.05 wt.% when it is discharged to 0.01 V, which is lower than that of ce-V₅S₈. As the battery is fully recharged back to 3.0 V, the loss of sulfur species for the ce-V₅S₈-C anode drops to 0.95 wt.%, while that of ce-V₅S₈ is 1.36%.

There are three main reasons responsible for the lower S-dissolution observed in the ce-V₅S₈-C anode case: 1) the strong electronic coupling between ce-V₅S₈ nanosheets and amorphous C layer enables a stable structure; 2) metal V particles act as pinning sites for the Na₂S, not only impeding S-dissolution but also enhancing electrical conductivity; 3) amorphous C layer overcoated on the surface of ce-V₅S₈ nanosheets acts as a barrier to reduce the contact between electrolyte and sulfide, thus alleviating Na₂S dissolution and improving structural stability and capacity at the full sodiation state.

Notes and references

S1. H. S. Matte, A. Gomathi, A. K. Manna, D. J. Late, R. Datta, S. K. Pati and C. N. Rao, *Angew. Chem. Int. Ed.*, 2010, **49**, 4059.

S2. P. G. Li, M. Lei, X. F. Wang, H. L. Tang and W. H. Tang, *J. Alloy. Compd.*, 2009, **474**, 463.

S3. K. Chang and W. Chen, *ACS Nano*, 2011, **5**, 4720.

S4. S. Ji, Z. Yang, C. Zhang, Z. Liu, W. W. Tjiu, I. Y. Phang, Z. Zhang, J. Pan and T. Liu, *Electrochim. Acta*, 2013, **109**, 269.

S5. W. Fang, H. Zhao, Y. Xie, J. Fang, J. Xu and Z. Chen, *ACS Appl. Mater. Interfaces*, 2015, **7**, 13044.

S6. R. Sun, Q. Wei, Q. Li, W. Luo, Q. An, J. Sheng, D. Wang, W. Chen and L. Mai, *ACS Appl. Mater. Interfaces*, 2015, **7**, 20902.

S7. J. Yang, J. Wang, Y. Tang, D. Wang, X. Li, Y. Hu, R. Li, G. Liang, T.-K. Sham and X. Sun, *Energy Environ. Sci.*, 2013, **6**, 1521.

S8. X.Z. Liao, Z.F. Ma, Q. Gong, H.L. Pei and L.J. Zeng, *Electrochem. Commun.*, 2008, **10**, 692.

S9. F. H. Zheng, C. H. Yang, X. Ji, D. L. Hu, Y. Chen and M. L. Liu, *J. Power Sources*, 2015, **288**, 337.

S10. Y. Xia, B. B. Wang, X. J. Zhao, G. Wang and H. Wang *Electrochim. Acta*, 2016, **187**, 55.

S11. M. Demeter, M. Neumann and W. Reichelt, *Surf. Sci.*, 2000, **454**, 41.

S12. G. Silversmit, D. Deplaa, H. Poelmana, G. B. Marinb and R. D. Gryse. *J. Electron.*

Spectrosc. Relat. Phenom., 2004, **135**, 167.

S13. Y. Wen, K. He, Y. J. Zhu, F. D. Han, Y. H. Xu, I. Matsuda, Y. Ishii, J. Cumings and C. S. Wang, *Nat. Commun.*, 2014, **5**, 4033.

S14. X. L. Wang, G. Li, M. H. Seo, F. M. Hassan, M. A. Hoque, Z. W. Chen, *Adv. Energy Mater.*, 2015, **5**, 1501106.

S15. X. Yang, R. Y. Zhang, N. Chen, X. Meng, P. L. Yang, C. Z. Wang, Y. Q. Zhang, Y. J. Wei, G. Chen and F. Du, *Chem. Eur. J.* 2016, **22**, 1445.